Publications of the Astronomical Society of Australia (2025), **42**, e165, 11 pages
doi:10.1017/pasa.2025.10124

Check for updates

CAMBRIDGE
UNIVERSITY PRESS

Research Article

Study on the subpulse drifting and nulling in PSR J1919+1745

Tao Yang[1], Xin Xu[1], Jie Tian[1], Jiguang Lu[2,3] and Qijun Zhi[1]

[1]School of Physics and Electronic Science, Guizhou Normal University, Guiyang, China, [2]CAS Key Laboratory of FAST, National Astronomical Observatories, Chinese Academy of Sciences, Beijing, China and [3]Guizhou Radio Astronomy Observatory, Chinese Academy of Sciences, Guiyang, China

Abstract

High-sensitivity observations of PSR J1919+1745 were conducted using the Five-hundred-metre Aperture Spherical Radio Telescope (FAST) at a central frequency of 1 250 MHz, enabling a detailed investigation of its single-pulse behaviour. Our research indicates that this pulsar is a normal pulsar, exhibiting null behaviour, subpulse drifting, and occasional bright pulses. Moreover, we observed that the null events tend to be of short duration, with an estimated overall null fraction of approximately $29.5 \pm 1.1\%$. Through Sliding Fluctuation Spectrum analysis, the modulation period of subpulse drifting is determined to be $P_3 = (6.1 \pm 0.7)P_1$ (where P_1 denotes the pulsar rotation period), and a non-drifting behaviour is also observed besides this. Analysis using the Harmonic-Resolved Fourier Spectrum indicates that a combination of amplitude modulation and phase modulation causes the subpulse drifting behaviour of this pulsar. Furthermore, the value P_2, derived from phase modulation, is approximately $360^\circ/21 = 17.1^\circ$. polarisation analysis shows a moderate degree of linear polarisation ($37.22 \pm 0.59\%$), an S-shaped swing in the polarisation position angle, and an approximate 90° orthogonal polarisation jump. The radiation characteristics of PSR J1919+1745 will expand the sample of pulsars with pulse null and subpulse drifting, thus contributing to future systematic studies on the physical origins of pulse null and subpulse drifting phenomena.

Keywords: Pulsars; PSR J1919+1745; single pulse

(Received 24 July 2025; revised 27 October 2025; accepted 4 November 2025)

1. Introduction

Pulsars are rapidly rotating and highly magnetised neutron stars. Owing to their strong magnetic fields and continuous emission of electromagnetic waves, a series of regular or discrete pulses is received when the radio beam emitted by the rotating pulsar sweeps across the telescope. These pulses exhibit interesting phenomena, such as subpulse drifting (Drake & Craft 1968; Cordes 1975) and nulling (Backer 1970a), but the causes are still not clear. So far, an increasing number of pulsars have been discovered (Zhi et al. 2024; Xu et al. 2025*b*; Han et al. 2025), and the population with nulling and subpulse drifting behaviours is extending, which includes some special phenomena such as multi-drifting behaviours and mode changing (Zhi et al. 2023; Xu et al. 2024*a*; Tian et al. 2024).

The 'nulling' phenomenon refers to the sudden cessation of pulsar radio emission for a certain period of time. It was first discovered by Backer (1970*a*). The duration of null pulses ranges from a few rotation periods to hundreds or even thousands of rotation periods. The null fraction (NF) describes the proportion of time a pulsar behaves in a null state, with observed NF values in null pulsars ranging from less than 1% to greater than 95% (Wang, Manchester, & Johnston 2007). In some cases, the transitions between emission states are periodic. Periodic null has been observed in many pulsars (e.g. Rankin & Wright 2007; Herfindal & Rankin 2007; Herfindal & Rankin 2009; Basu, Mitra, & Melikidze 2017; Rahaman et al. 2021). In some cases, the emission state transitions are periodic. The periodic nulling observed in many pulsars is very similar to periodic non-drifting amplitude modulation. Therefore, Basu et al. (2017) speculated that the two may originate from the same physical mechanism. The null phenomenon has been observed in pulsars for several decades, with over 200 pulsars reported to exhibit null behaviour (Wang et al. 2020). Despite this, the physical mechanisms underlying the transitions between these two states remain unclear.

Subpulse drifting is another significant phenomenon observed in pulsars, characterised by the systematic movement of subpulses within the pulse window. Since its discovery by Drake & Craft (1968), subpulse drifting has been detected in hundreds of pulsar observations (Weltevrede, Edwards, & Stappers 2006; Weltevrede, Stappers, & Edwards 2007; Basu et al. 2019), indicating that this phenomenon is relatively common among pulsars. Three parameters are used to describe the observed subpulse drifting: the horizontal time interval between adjacent drifting bands (P2, in units of degrees (°)), the vertical band spacing at the same pulse phase (P3, in units of the pulsar's rotation period (P_1)), and the drifting rate ($\Delta\phi = P_2/P_3$, in units of $^\circ/P_1$; Smits, Mitra, & Kuijpers 2005). The carousel model, initially proposed by Ruderman & Sutherland (1975), has been widely used to explain the drifting subpulse phenomenon in pulsars. In this model, the radiation is produced by a series of 'sparks' that rotate around the magnetic axis with a fixed period. As these 'sparks' rotate through the observer's line of sight, they produce the characteristic drifting subpulses observed in many pulsars. Although the model effectively accounts for some observed subpulse drifting in pulsars,it struggles to explain more complex subpulse drifting phenomena. To address the diversity of subpulse drifting, multiple models have been proposed. The quasi-radial spark model by

Corresponding author: Qijun Zhi, Email: qjzhi@gznu.edu.cn

Cite this article: Yang T, Xu X, Tian J, Lu J and Zhi Q. (2025) Study on the subpulse drifting and nulling in PSR J1919+1745. *Publications of the Astronomical Society of Australia* **42**, e165, 1–11. https://doi.org/10.1017/pasa.2025.10124

Gil & Sendyk (2000) indicates that pulsar polar caps have multiple non-random spark regions, accounting for non-drifting core components in some pulsar profiles. The modified carousel model by Szary et al. (2022), assuming sparks rotate around the polar cap potential maximum, clarifies drift rate reversals in several pulsars. Basu et al. (2023) partially screened gap (PSG) model, addressing the polar cap's intricate magnetic structure and strong non-dipole fields, offers a novel perspective on subpulse drifting and enhances our understanding of pulsar magnetosphere configuration and radiation mechanisms. However, no single model can explain all subpulse drifting phenomena. Therefore, observing and statistically studying more subpulse drifting pulsars to summarise their characteristics is crucial for refining pulsar radiation models.

With the advent of high-sensitivity telescopes, a variety of intriguing subpulse drifting phenomena have been increasingly discovered, including bi-drifting (Szary et al. 2020), multiple drift modes (McSweeney et al. 2019; Zhi et al. 2023), and drift direction reversals (Biggs et al. 1985; Xu et al. 2024a), many of which were not previously observed. PSR J1919+1745, initially classified as a Rotating Radio Transient (RRAT) (Deneva et al. 2009), has garnered significant attention. Recent findings by Ren et al. (2024) report a relatively high proportion of burst pulses, leading to the hypothesis that it may either be a quiescent pulsar or a weak pulsar exhibiting sporadic but intense emissions. Subsequent observations of this pulsar as part of the FAST GPPS survey (Zhou et al. 2023) revealed pulsar-like behaviour during a five-minute integration, thanks to the exceptional sensitivity of Five-hundred-meter Aperture Spherical Radio Telescope (FAST). However, the precise characteristics of its individual pulses remain unclear. Consequently, high-sensitivity, long-duration observations are essential to better understand its single-pulse behaviour.

In this paper, we present the results of single-pulse observations of PSR J1919+1745 conducted with the FAST at a central frequency of 1 250 MHz. Provide a detailed report on its subpulse drifting behaviour and polarisation properties. The structure of this paper is as follows: Section 2 introduces the FAST observations of PSR J1919+1745 and the data processing methods; Section 3 presents the analysis results for this pulsar; Section 4 provides a discussion and conclusions.

2. Observations and data processing

On September 21, 2023, we conducted approximately 90 min of observations of PSR J1919+1745 using the high-sensitivity FAST telescope. The observation utilised the central beam of the 19-beam receiver, covering a frequency range from 1 000 to 1 500 MHz. The data were recorded in the SwiftCalibration mode PSRFITS format Hotan van Straten, & Manchester (2004), which includes full Stokes information, 8-bit sampling, a time resolution of 49.152 ms, and 1 024 frequency channels. Using the timing ephemeris provided by the ATNF Pulsar Catalogue (PSRCAT V-1.67) (Manchester et al. 2005), we folded the data into 1 024 phase bins per pulse period using the DSPSR software package (Hotan et al. 2004; van Straten & Bailes 2011) to obtain single-pulse profiles. A total of 2 594 individual pulses were obtained. Owing to the effects at the band edges, the analysis was restricted to the frequency range of 1 050–1 450 MHz (Jiang et al. 2020). During the observation, the radio signals from the pulsar are typically contaminated, to a greater or lesser extent, by narrowband non-pulsar radio emission at some frequencies. This narrowband non-pulsar radio frequency interference (RFI) was identified and removed using the PAZ and PAZI commands in the PSRCHIVE software package (Hotan et al. 2004; van Straten, Demorest, & Oslowski 2012). Of course, the superior geographical location and favourable radio observing conditions of FAST mean that the removal of a small amount of RFI did not significantly alter the signal-to-noise ratio (SNR) of the detected signal. polarisation calibration was achieved using the PAC command in the PSRCHIVE software package, through the noise signal.

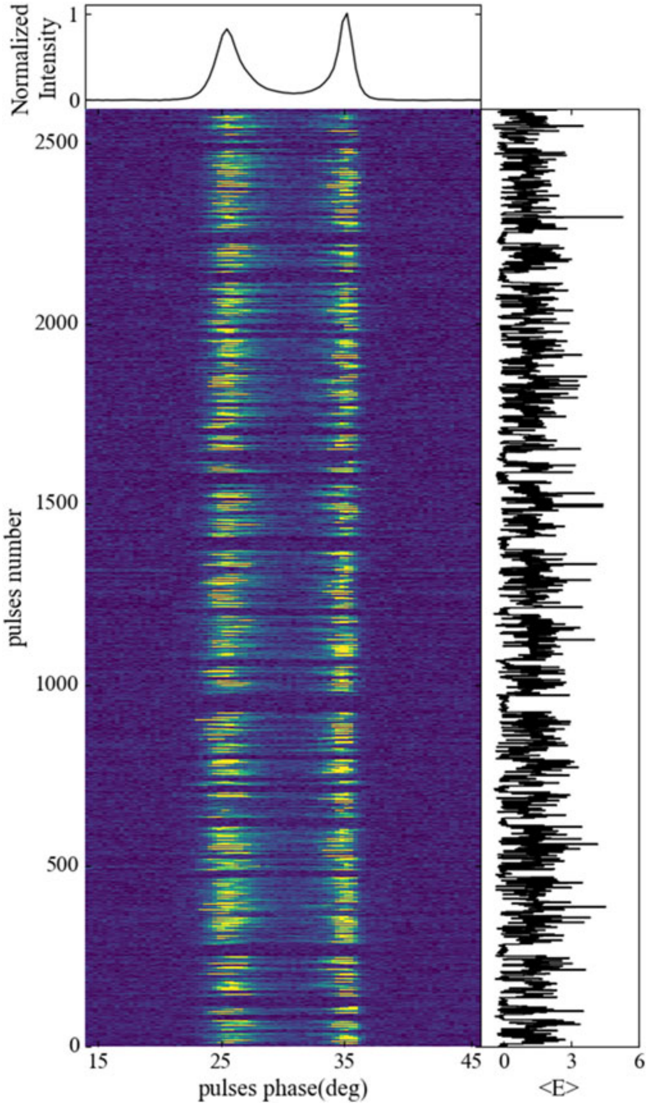

Figure 1. The main panel displays the sequence of 2 594 single pulses that we observed. The upper panel shows the normalised integrated pulse profile, while the right panel illustrates the variation of pulse energy within the pulse sequence, with energy values normalised to the mean energy.

3. Results

Observation data from a high-sensitivity telescope are helpful for further studying the single-pulse behaviour of pulsars. In this section, the observation results of the high-sensitivity telescope FAST on PSR J1919+1745 will be shown, including nulling, bright pulses, and single-pulse modulation. Those phenomena are displayed in Figure 1. Next, we will analyse them one by one.

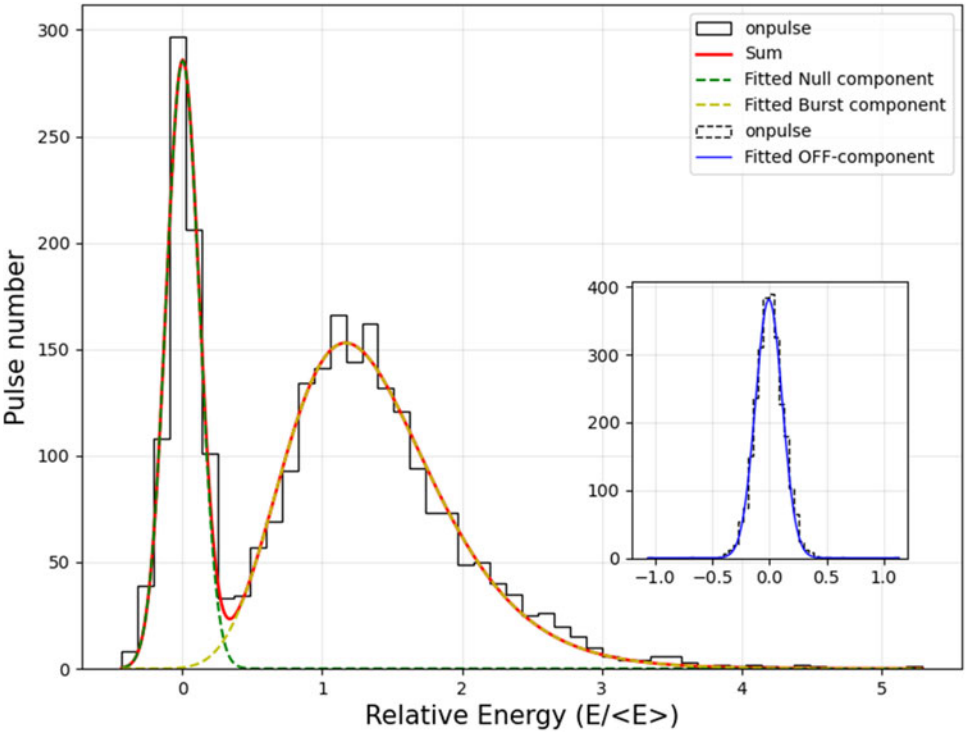

Figure 2. Pulse energy histograms are presented for the on-pulse (solid black line) and off-pulse (dashed black line) windows. The energy values have been normalised by the mean pulse energy. The pulse energy distribution in the pulsing window is composed of a combination of Gaussian and log-normal components (solid red line). The evident double-peaked structure arises from the presence of null and burst states.

3.1. Single-pulse sequence and energy distribution

The single-pulse sequence of pulsar J1919+1745 was investigated through the analysis and processing of the obtained data. The pulse stack of the 2 594 single pulses of PSR J1919+1745 in our observation is shown in Figure 1. The upper panel shows the corresponding normalised integrated pulse profile, which consists of two components, with the leading component being slightly lower than the trailing component. The right panel shows the corresponding on-pulse energies, which are calculated by summing the intensities within the pulse phase interval of the integrated pulse profile for each pulse and have been normalised by the average on-pulse energy. Figure 1 indicates that there are segments within the entire pulse sequence where no pulse emission was detected (e.g. pulse numbers 920–970; pulse numbers 1 370–1 410; pulse numbers 2 220–2 250), a phenomenon referred to as pulse null. This suggests that PSR J1919+1745 switches between the null state and the burst state. Owing to the extremely high sensitivity of FAST, PSR J1919+1745 behaves like an ordinary pulsar, although occasional bright pulses or null events occur. It can be understood that when the detection threshold is tens or even hundreds of times higher than the current 3σ threshold of FAST observations, only a few strong pulses will be detected and are likely to be classified as RRATs, as described in the original discovery paper (Deneva et al. 2009).

To further investigate the single-pulse emission frequency of J1919+1745, we followed the prescription of Ren et al. (2024) and derived a burst rate of 1 225~h^{-1}, which is significantly higher than the 847~h^{-1} reported with the Parkes telescope (Ren et al. 2024) and the 320~h^{-1} obtained with the Arecibo telescope (Deneva et al. 2009). Owing to the exceptional sensitivity of FAST, a considerably larger population of previously undetectable faint pulses can now be reliably identified.

The pulse energy distributions for the on-pulse and off-pulse windows are shown in Figure 2. The pulse energy of individual pulses was obtained by summing the intensities of each single pulse within the on-pulse phase range of the integrated pulse profile. The on-pulse region was defined as the range over the entire longitude where significant pulse emission was detected. Similarly, for the calculation of off-pulse energy, we used a window of the same length as the on-pulse window and selected a stable baseline, following the aforementioned method to calculate the off-pulse energy for each single pulse. After normalisation by the mean pulse energy, the on-pulse energy of individual pulses is represented by the black histogram.

To characterise these distributions, we fitted the energy distribution in the pulse region to a combination of a Gaussian function and a log-normal function. The fitting results are shown as the red curve in Figure 2. The distribution of the quiescent state follows a Gaussian distribution centred at zero, while the distribution of the burst state follows a log-normal distribution.

$$Y(E) = \frac{A}{E\sigma\sqrt{2\pi}} \exp\left[-\frac{(\ln(E)-\mu)^2}{2\sigma^2}\right] \tag{1}$$

Here, A, μ, and σ represent the normalisation factor, the logarithmic mean, and the standard deviation of the distribution, respectively. We applied the Kolmogorov–Smirnov (KS) hypothesis test to the pulse energy distribution to examine whether it conforms to a log-normal distribution. The p -value obtained from

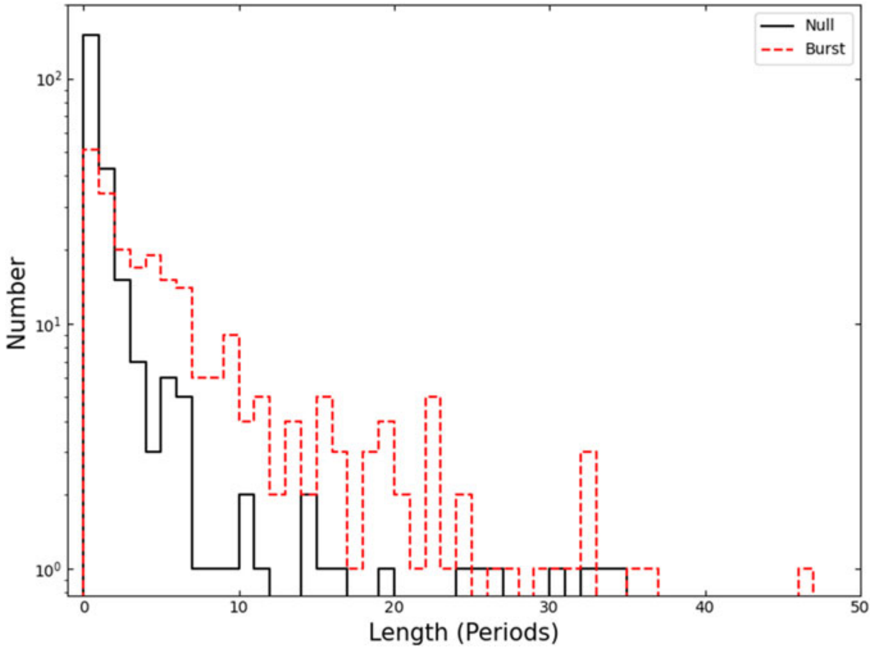

Figure 3. The distributions of the durations of the null (Black dotted line) and the burst (red solid line) states for PSR J1919+1745.

the KS test is 0.39, which is greater than the threshold of 0.05, indicating that the pulse energy distribution is consistent with a log-normal distribution.

3.2. Nulling behaviour

Identifying the burst and null states is essential for further investigation of the properties of the burst and null pulses. To distinguish between null and burst pulses, we adopted the method proposed by Bhattacharyya, Gupta, & Gil (2010), which suggests that the uncertainty of each pulse energy is determined by $\sigma_{ep} = \sqrt{n_{on}}\sigma_{off}$, where n_{on} is the number of bins in the on-pulse window and σ_{off} is the rms of the off-pulse region for individual pulses. Owing to the high sensitivity of FAST, we selected a 3σ threshold. Pulses with energies below this threshold were categorised as null pulses, whereas pulses with energies above this threshold were classified as burst pulses.

Based on the identified null and burst pulses (the burst and null states), we estimated the NF of PSR J1919+1745, obtaining an NF value of 29.5 ± 1.1%. The uncertainty of the NF was calculated using the formula $\sqrt{n_p}/N$, where n_p and N represent the number of null pulses and the total number of single pulses, respectively (Wang et al. 2007).

Furthermore, we calculated the durations of the null and burst states, with the results presented in Figure 3. The results show that the durations of both the null and burst states are predominantly very short, with the majority falling within the range of 1–2 pulse periods. This characteristic suggests that the pulsar frequently switches between the burst and null states within 1–2 rotation periods. It is noteworthy that while the typical duration of the null state is less than 7 pulse periods, the maximum duration of the null state exceeds 30 pulse periods. The typical duration of the burst state is less than 23 pulse periods, although the maximum duration of the burst state reaches as high as 47 pulse periods.

To investigate whether the observed null pulses were actually weak emission pulses, we separately folded the null and burst pulses to obtain their integrated pulse profiles, as shown in Figure 4. The upper panel displays the integrated pulse profile of the null pulses, while the lower panel shows the integrated pulse profile of the burst pulses, with the profiles normalised. In the upper panel, the mean profile of the null pulses does not exhibit any significant emission components, indicating the absence of detectable radiation during the null state.

In previous studies, the periodicity of pulsar null behaviour has often been investigated (Basu et al. 2017; Rejep et al. 2022). To examine whether the null behaviour of PSR J1919+1745 is periodic, we employed the method described by Basu et al. (2017). Initially, we labelled burst pulses as 1 and null pulses as 0, thereby generating a 1–0 sequence. Subsequently, we applied a one-dimensional Discrete Fourier Transform (DFT) to a continuous time series consisting of 256 points. For each subsequent sequence, the starting position was shifted by 10 pulse periods, and this process was repeated until the end of the time series data was reached. Finally, we averaged the individual DFTs to determine the periodicity of the pulsar's null behaviour. The results are shown in Figure 5, with the main plot displaying the temporal variation of the DFT and the bottom plot showing the average DFT over the entire observation period. During the entire observation duration, there is a weak periodic signal corresponding to around 70 pulses (see figure below). However, this periodicity is not statistically significant. Longer-term observations are required to confirm the periodicity of this pulsar's state transitions.

3.3. Bright pulses

In this study, we adopted the method proposed by Tedila et al. (2022) to investigate the bright pulse events of PSR J1919+1745. This approach categorises a pulse as bright when its peak intensity surpasses ten times the mean value. During the 1.5-h observation,

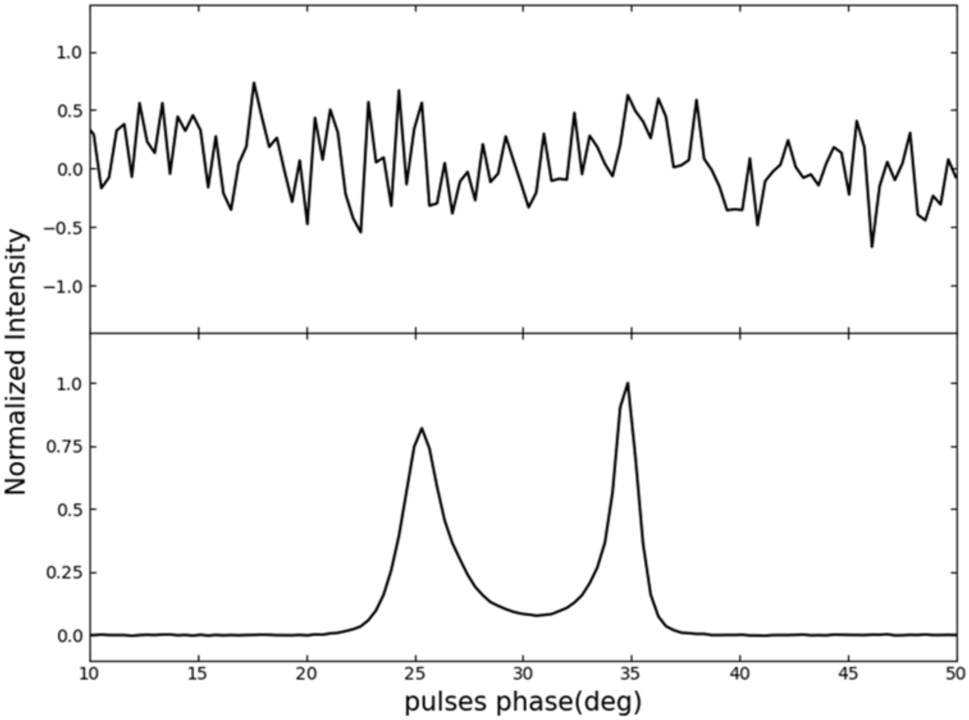

Figure 4. The mean pulse profiles of PSR J1919+1745 for the null (top panel) and the burst states (bottom panel).

a total of 19 bright pulses were detected, accounting for approximately 0.7% of all single pulses. Three of these were identified in the leading component, while the remaining were detected in the trailing component. Notably, no instances were found where pulses with peak intensities exceeding ten times the mean value were simultaneously detected in both the leading and trailing components. Figure 6 presents the integrated pulse profiles of bright pulses detected in both the leading and trailing components, alongside the positions of their peak intensities relative to the integrated pulse profile throughout the entire observation period. For bright pulses in the leading component, their intensity peaks predominantly appear at later pulse phases corresponding to the peak of the leading component. Conversely, the peak intensities of bright pulses in the trailing component are predominantly located at earlier pulse phases within the trailing component.

3.4. Single-pulse modulation

To investigate the single-pulse modulation behaviour in PSR J1919+1745, we employed the Sliding Fluctuation Spectrum (SFS; Maan & Deshpande 2014). The SFS is generated by applying the Localized Random Fourier Spectrum (LRFS; Backer 1970*b*) to blocks of M pulses and calculating the spectra. The spectra are horizontally folded to produce a one-dimensional curve. Subsequently, the DFT 'window' is shifted by one pulse, and the entire process is repeated. Applying the sliding DFT window to the pulse stack generates N - M + 1 curves, which are stacked together to produce the so-called 'collapsed wavelet spectrum'. The length of the DFT window is crucial for the resolution and sensitivity of the map. A window that is too small results in insufficient spatial resolution in the P_0/P_3 space, making details indistinguishable. Conversely, a window that is too large reduces sensitivity, causing transient events to be less prominent on the map and lowering the SNR.

As shown in Figure 7, the SFS of all pulse sequences from PSR J1919+1745 is presented, with a DFT window size of 128 pulses. Two features primarily dominate the wavelet spectrum. The left panel displays the temporal variation of modulation power obtained by integrating these two features (normalised), while the bottom panel shows the LRFS along the y-axis. The modulation period was determined to be $P_3 = (6.3 \pm 1.2)P_1$ by fitting a Gaussian function near the main peak of the LRFS. Two notable features can be highlighted from this figure. First, low-frequency modulation significantly modulates the power across the entire pulse profile, with the wavelet spectrum being dominated by components similar to white noise (e.g. initial cycle numbers ranging from 0 to 700). Second, the frequency of high-frequency modulation varies continuously, with unstable periodicity that is only present in certain pulse sequences. We identified pulse sequences with clear periodic modulation from 1 800 to 1 934,1463 to 1 570, and 1 144 to 1 322. The pulse stacks of these three pulse sequence segments are shown in Figure 8.

While the SFS provides rich information about the fluctuations in the pulse sequence, it samples the fluctuations only once per pulse period at a given longitude. This characteristic may lead to aliasing issues. To determine whether the observed fluctuation characteristics are caused by aliasing from fluctuations with frequencies higher than 0.5 cycles/P_1, the fluctuations must be sampled at a rate higher than once per period. This can be achieved by taking advantage of the fact that the fluctuations are sampled only within the finite width of the pulse. To this end, before unfolding the single-pulse stack, the values within the sampled (off-pulse) regions were retained, while the unsampled (on-pulse) regions were filled with zeros. Subsequently, the pulse stack was

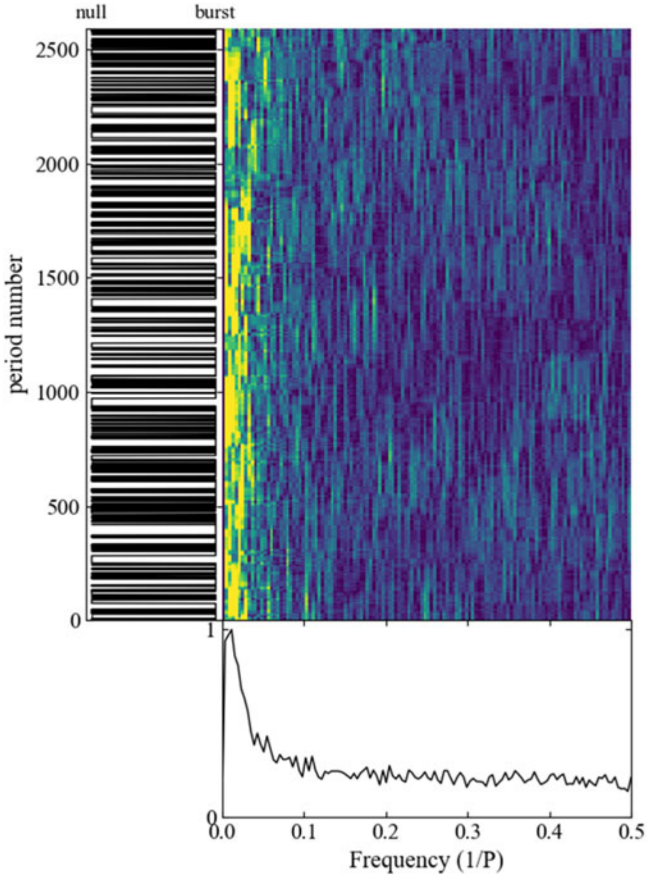

Figure 5. The figure displays the time-varying Fourier transform of the null/ burst (zero/one) time series data. In the left panel, the identified emission states corresponding to each period are depicted, while the bottom panels show the average DFT for the entire observation. The right panel illustrates the time evolution of the DFT corresponding to the null/burst time series. Throughout the observation, a weak periodicity of approximately 70 pulses was detected.

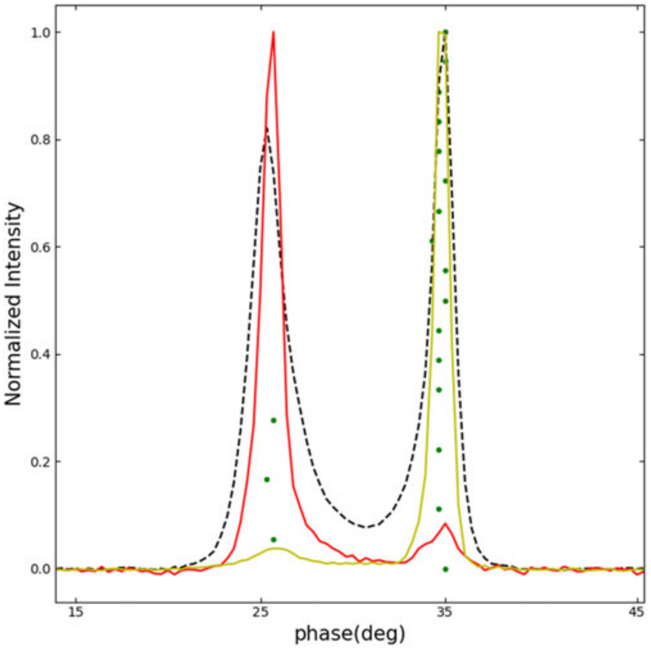

Figure 6. Plot showing the integrated pulse profiles for the bright pulses found in the leading (red) and trailing (yellow) components, and the locations for the peak intensity (green dots) relative to the integrated pulse profile (dashed black).

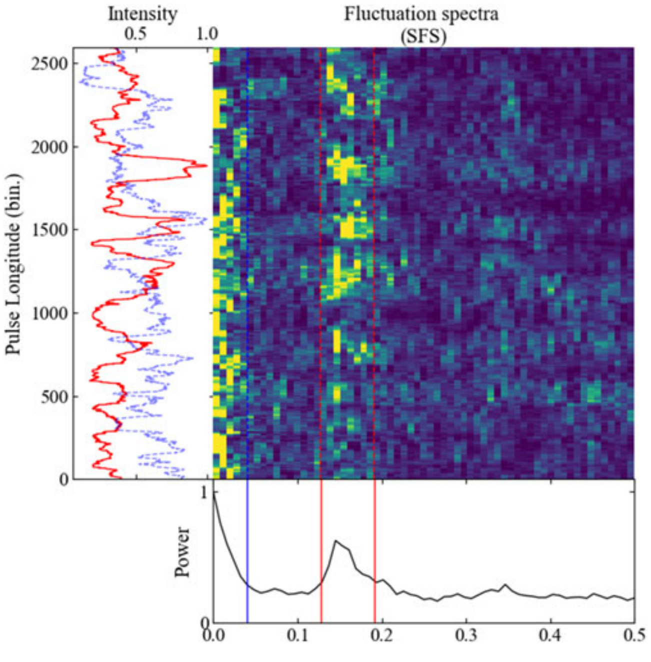

Figure 7. Display showing the time evolution of the LRFS in the PSR J1919+1745. The left panel shows the time variation of the modulation power by integrating low-frequency (blue) and high-frequency (red) features. The two modulation features are distinguished by the dashed lines. The bottom panel shows the time average LRFS.

unfolded into a reconstructed time series by arranging the individual pulses in sequential order, thereby forming a continuous time series. A Fourier transform was then applied to this constant time series to obtain an unexpanded wavelet spectrum. Finally, the continuous slices of the unexpanded wavelet spectrum, each spanning P_1 (one period), were superimposed to form a series of overlapping bands, resulting in the Harmonic-Resolved Fourier Spectrum (HRFS; Deshpande & Rankin 2001). The HRFS can also distinguish between the two types of modulation encountered, namely amplitude modulation and phase modulation. For example, the integrated spectrum will exhibit nearly symmetric features in the case of amplitude modulation, while a clear asymmetry would be apparent for phase modulation.

Figure 9 presents the HRFS of these three pulse sequence segments with clear periodic modulation to decipher the phase nature of the subpulse drifting. The left panel displays the spectral power at a frequency of one harmonic per P_1 period and its higher harmonics, with the harmonic number representing the continuous segments per P_1 period. The middle panel's colour scale map shows the complete wavelet power spectrum, while the bottom panel presents the integrated power spectrum. The low-frequency modulation features evident in the LRFS analysis appear to vanish entirely in the HRFS analysis. Corresponding to the LRFS, high-frequency modulation features emerge in the HRFS with a peak around $f_p = 0.158$ cpp, $P_3 = (6.1 \pm 0.7)P_1$ (obtained by averaging the three data segments), indicating that the subpulses are gradually drifting towards the leading edge. However, the asymmetry of the high-frequency modulation feature is not pronounced, suggesting that the high-frequency modulation is caused

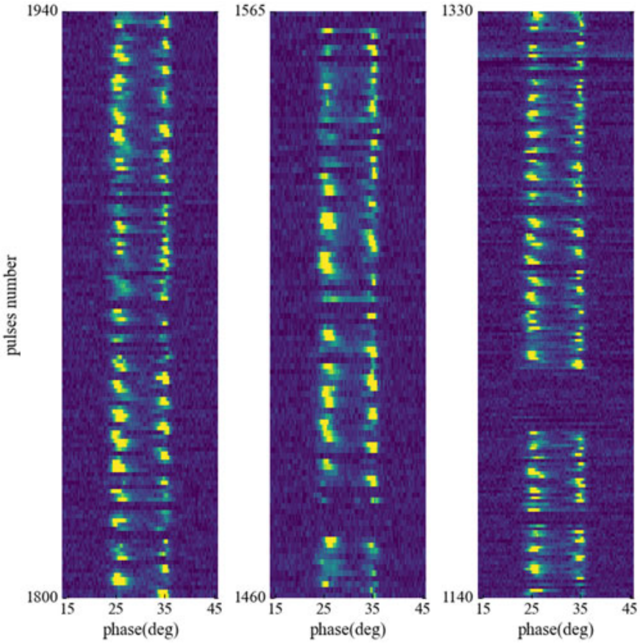

Figure 8. The pulse stacks of the three pulse sequence segments with clear periodic modulation.

by a combination of amplitude modulation and phase modulation, with both types of modulation being mixed. Additionally, it is noteworthy that the amplitude of the high-frequency modulation feature reaches its maximum at approximately the 21st harmonic number, implying that the P_2 value, derived from phase modulation, is approximately $360^\circ/21 = 17.1^\circ$.

3.5. Polarisation characteristics

Figure 10 shows the polarisation profiles and the polarisation position angle (PPA) of 6 single pulses of PSR J1919+1745, each with a SNR higher than 50. The upper part of the figure presents the variation of PPA with phase, while the lower part shows the variation of normalised intensity with phase, including three polarisation components: I (total intensity, black solid line), L (linear polarisation, red dashed line), and V (circular polarisation, blue dotted line). As can be seen from Figure 10, the intensities of the two peaks in the single-pulse polarisation of PSR J1919+1745 exhibit significant differences and a relatively wide variation range. Specifically, in the top three subplots, the PPA curves of these three single pulses show an S-shaped swing. Among them, the pulse region of the 576th pulse (top right) is relatively wide, spanning approximately 23°–36°. In the bottom three subplots, however, the positions of the PPAs are relatively scattered. The 1 492nd pulse (bottom left) exhibits an obvious orthogonal jump phenomenon; the pulse region of the 2 354th pulse (bottom right) is relatively narrow, ranging from approximately 34.5° to 36.2°.

The left panel of Figure 11 displays the integrated pulse profile and polarisation information of PSR J1919+1745 at 1 250 MHz during this observation, to understand its underlying radiation mechanism. To eliminate the effects of the pulsar ionosphere and interstellar medium during propagation, we corrected the integrated pulse profile using the rotation measure (RM) value determined by the RMFIT software package. The final RM of the pulsar was determined to be 522.2 ± 3.9 rad m^{-2}. The integrated polarisation profile of PSR J1919+1745 exhibits moderate linear polarisation with a degree of linear polarisation of $37.22 \pm 0.59\%$. The degree of circular polarisation is $2.4 \pm 0.32\%$, with little evidence of significant circular polarisation. The upper part of the left panel in Figure 11 displays the linear PPA curve of the integrated profile within the pulse window (error bars in red). It can be observed that the PPA curve exhibits an S-shaped swing and undergoes a jump of 90°. This S-shaped swing can be well explained by the rotating vector model (RVM) proposed by Radhakrishnan & Cooke (1969). We fitted the observed PPA curve with the RVM:

$$\tan\left(\psi - \psi_0\right) = \frac{\sin\alpha\,\sin\left(\phi - \phi_0\right)}{\sin\zeta\,\cos\alpha - \cos\zeta\,\sin\alpha\,\cos\left(\phi - \phi_0\right)} \tag{2}$$

Where α is the angle between the magnetic axis and the rotation axis; $\zeta = \alpha + \beta$ is the angle between the line of sight and the rotation axis, where β is the impact parameter, that is, the angle between the line of sight and the magnetic axis at the point of closest approach; ψ_0 and ϕ_0 are the polarisation angle and pulse longitude, respectively, at the steepest point of the polarisation angle curve. The red curve in the upper panel of Figure 11 represents the best fit to the polarisation angle obtained using the RVM model.

In the right panel of Figure 11, we present the variation of the normalised χ^2 values with the magnetic inclination angles α and β. For this pulsar, the results of the RVM fitting can constrain the range of β to $4.5^\circ > \beta > 0^\circ$, while no constraint on α can be achieved. Additional constraints on these parameters will be elaborated in detail in the Discussion section.

4. Discussion and conclusions

We conducted high-sensitivity observations of PSR J1919+1745 using the FAST telescope, presenting the first detailed report on its single pulse behaviour and polarisation features at 1.25 GHz. The data reveal that the pulsar does not exhibit significant RRAT characteristics, supporting its classification as a normal pulsar. Notably, we observed pronounced nulling with a NF value of $29.5\% \pm 1.1\%$, as well as subpulse drifting with a repetition period of $P_3 = (6.1 \pm 0.7)P_1$. The pulsar also shows occasional high energy bright pulses. Due to sensitivity limitations, early observations (Deneva et al. 2009) likely captured only the brighter pulse segments, which may explain its initial misclassification as an RRAT.

The duration of nulling states is crucial for understanding the origin of pulsar radiation. Current research suggests that short nulling events may arise from the line-of-sight crossing gaps between adjacent sparks (Herfindal & Rankin 2009; Basu et al. 2017), often exhibiting high periodicity. Longer nulling durations likely reflect changes in the magnetospheric structure (Wang et al. 2007), such as disruptions in particle acceleration (Jones 1981), transitions in radiation mechanisms (Zhang, Qiao, & Han 1997), or changes in the magnetic field configuration (Timokhin 2010). Our observations show that null durations in PSR J1919+1745 typically span 1–2 pulse periods, with occasional extended nulling lasting over 10 pulse periods. These null states exhibit a significant quasi-periodicity of approximately 70 pulse periods, indicating that periodic nulling may be driven by underlying physical processes within the pulsar (Basu et al. 2019). We suggests that the

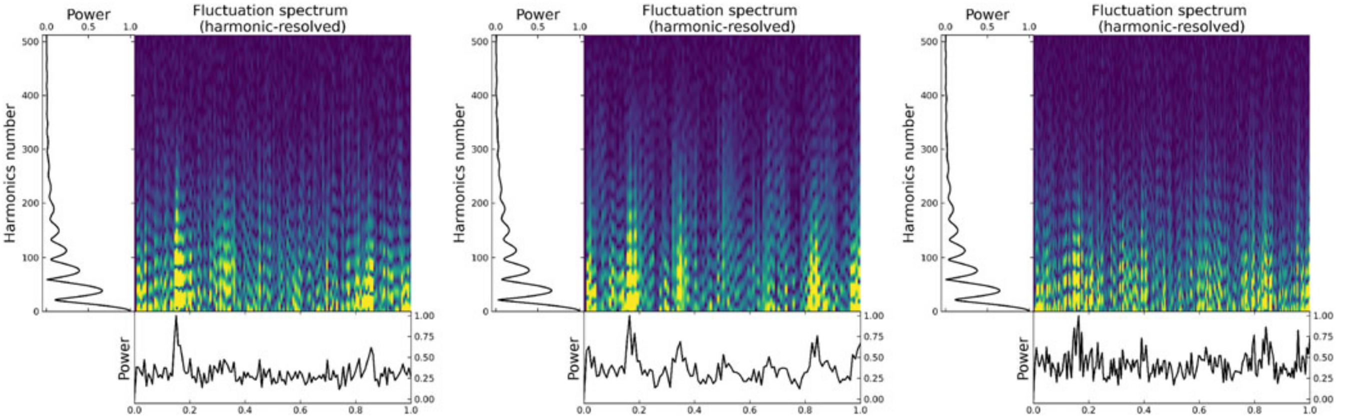

Figure 9. The HRFS of the three pulse sequence segments shown in Figure 8 is presented. The colour-coded plot in the main panel displays the full spectrum, while the bottom panel shows the harmonic-integrated spectrum. The left panel shows the amplitude of the harmonics at an integral multiple of the pulsar rotation frequency.

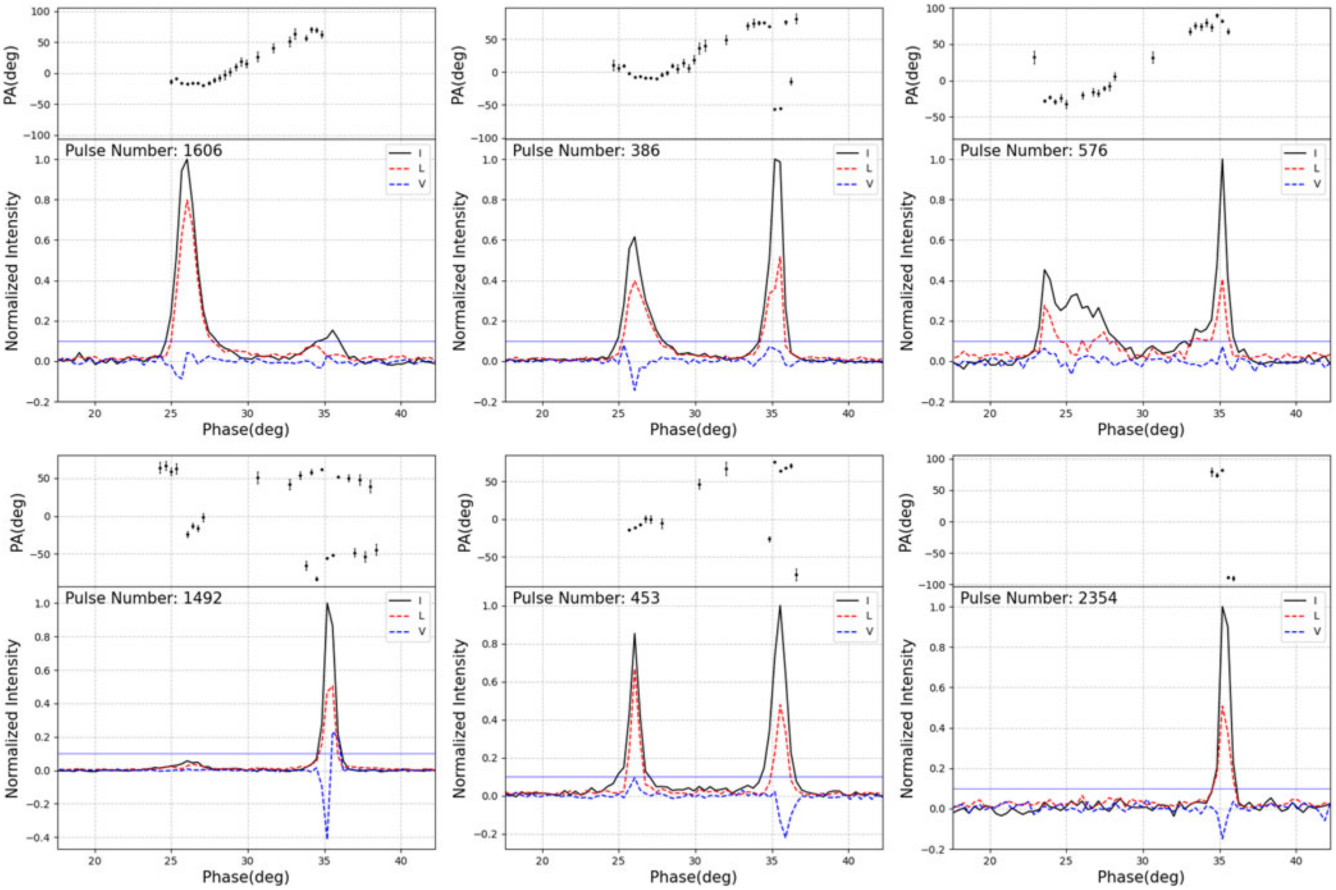

Figure 10. The single-pulse profiles of PSR J1919+1745.

nulling observed in this pulsar results from a combination of large-scale magnetospheric changes and mismatches in the line-of-sight spark geometry.

The subpulse drifting phenomenon is commonly explained by the classical carousel model, in which discrete emission regions rotate around the magnetic axis, giving rise to the observed subpulse drifting behaviour (Ruderman & Sutherland 1975). This model successfully accounts for the stable drifting behaviour seen in some pulsars (e.g. Bhattacharyya et al. 2007; Rankin & Rosen 2014). However, as the observational sample expands, more pulsars have been found to exhibit variations in their drifting behaviour, such as PSRs J0034-0721 (McSweeney et al. 2019),

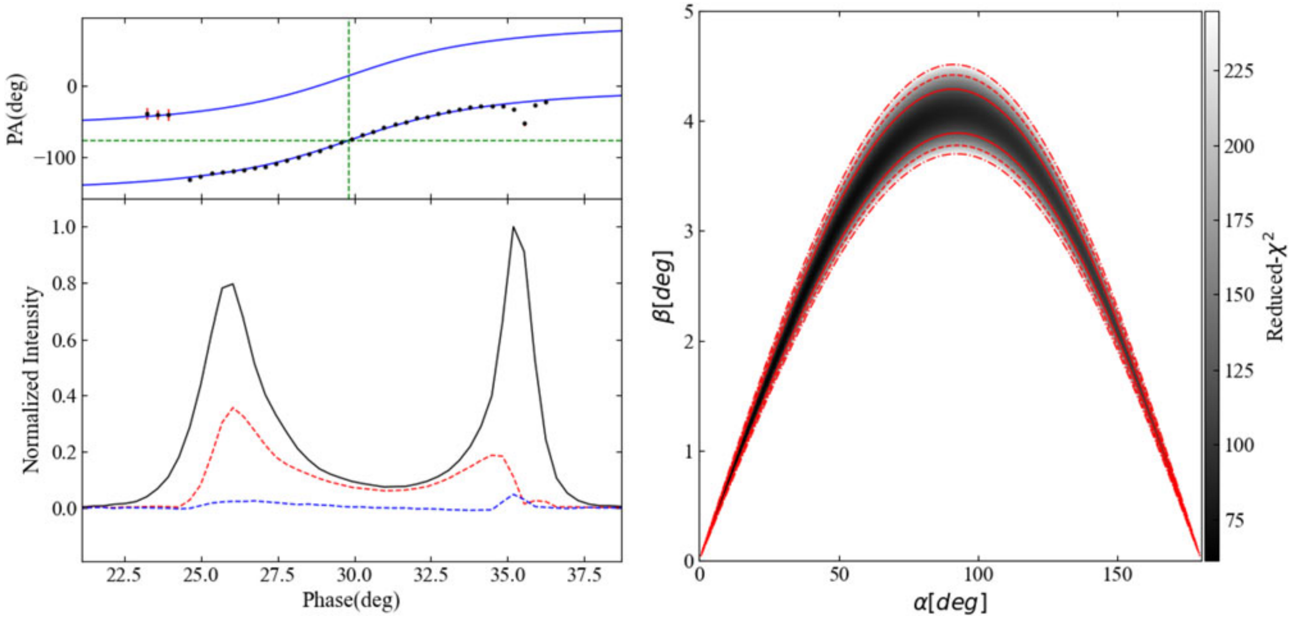

Figure 11. Left panel: the polarisation profile at 1 250 MHz. In the figure below, the black solid line represents the average flux profile, the red dashed line represents the linear polarisation profile, and the blue dashed line represents the circular polarisation profile. In the upper figure, the black dots indicate the linear polarisation angle, and the blue line represents the best-fit curve obtained from the rotating vector model (RVM) fitting. Right panel: the results of fitting an RVM curve for each (α, β) combination for the mean profile. The reduced chi-squared (χ^2) of the fit is depicted in grey scale, with the darkest shade indicating the optimal fit. Additionally, the red contour lines signify 1σ,2σ, and 3σ confidence boundaries, depicted as solid, dashed, and dotted–dashed lines, respectively.

J1727-2739 (Wen et al. 2016), and J2007+0910 (Xu et al. 2024b). In the case of PSR J1919+1745, our SFS analysis reveals that the pulsar occasionally exhibits subpulse drifting with a period of $P_3 = (6.1 \pm 0.7)P_1$, while at other times, nearly stable subpulse structures (i.e. non-drifting behaviour) are observed. Additionally, the HRFS analysis shows that the P_2 value corresponding to the drifting behaviour is 17.1°. Our results demonstrate that PSR J1919+1745 exhibits both drifting and non-drifting subpulse behaviour, challenging the traditional carousel model. Several models have been proposed to explain pulsar drift instability, including the partially shielded gap (PSG) model (Gil, Melikidze, & Geppert 2003; Szary, Melikidze, & Gil 2015, multiple magnetospheric states incorporating the apparent motion of the visible point (Yuen 2019), reconfiguration of the pulsar magnetosphere (Timokhin 2010), and aliasing effects caused by undersampling (McSweeney et al. 2019). However, there remains no consensus on the underlying cause of the observed changes in pulsar drifting behaviour.

The traditional carousel model suggests that if sparks above the polar cap are equidistant in magnetic azimuth, the subpulse drift behaviour is governed by the number of sparks, n, and the carousel rotation period, P_4. The theoretical value of P_4 can be derived from the following equation (Ruderman & Sutherland 1975):

$$P_4 = 5.7 \times \left(\frac{P_1}{s}\right)^{-3/2} \left(\frac{\dot{P}}{10^{-15}}\right)^{1/2} \tag{3}$$

The results is $P_4 = 2.5$. However, it is important to note that sampling once per pulse period may introduce aliasing in the observed subpulse drifting behaviour. The apparent drift is influenced by both the actual drifting and the sampling rate. In this case, the apparent repetition period can be expressed as (McSweeney et al. 2019):

$$\frac{1}{P3} = \left|\frac{n - kP_4}{P_4}\right| \tag{4}$$

where $k = [n/P_4]$ is the aliasing order, in which the square brackets denote rounding to the nearest integer. We propose that the coexistence of drifting and non-drifting behaviours in PSR J1919+1745 may be attributed to the aliasing effect. We considered first-order aliasing phenomena ($k \pm 1$), assuming that k is the same in both drifting and non-drifting states, and that the spark point counts follow equidistant sequences. Using the method described by Janagal et al. (2022), we derived the optimal solution. For $k = 1$, the subpulses exhibit drifting behaviour at $n = 5$ with a repetition period of approximately 6 P. At $n = 6$, the subpulses exhibit non-drifting behaviour. For $k = -1$, $n = 7$ and $n = 6$ correspond to drifting and non-drifting behaviour, respectively.

Previous studies suggest that pulsar radiation beams consist of a core component and several nested cone components (Rankin 1983, 1993a; Qiao & Lin 1998; Xu et al. 2025a). Integrating pulse profiles with polarisation data reveals the geometric structure of the radiation beam along the line of sight (Rankin 1993b). PSR J1919+1745 shows two distinct peaks at 1.25 GHz with moderate linear polarisation, accompanied by significant depolarisation at the profile edges. Its PPA curve shows a typical S-shaped swing, remaining relatively flat, consistent with the predictions of RVM (as shown in Figure 11). Furthermore, given that subpulse drifting is generally associated with the cone radiation component (Basu et al. 2016), this evidence supports the classification of PSR J1919+1745 as a conal-double profile pulsar (Rankin 1983).

Notably, a $\sim 90^\circ$ jump in the PPAs at the leading edge of the profile suggests the presence of two orthogonal polarisation modes (OPM, Manchester, Taylor, & Huguenin 1975; Backer, Rankin, & Campbell 1976). This may be linked to the pulsar's radio emission mechanism or to the two propagation modes (ordinary mode (O mode) and extraordinary mode (X mode)) inherent to the relativistic magnetised plasma within the pulsar's magnetosphere (Arons & Barnard 1986). The specific physical mechanisms driving the dominance of OPM in different regions of the pulse profile remain to be further investigated.

The radiation height of pulsars is crucial for understanding pulsar radiation geometry. Rookyard et al. (2015) pointed out that the RVM predicts that the inflection point (ϕ_0) of a pulsar's PPA curve should coincide with the fiducial plane phase ($\phi_{\rm fid}$). However, affected by the relativistic aberration/retardation (A/R) effect, ϕ_0 in actual observations often exhibits a delay relative to $\phi_{\rm fid}$, denoted as $\Delta\phi = \phi_0 - \phi_{\rm fid}$. The pulsar's emission height can then be derived using the formula

$$\Delta\phi = \frac{8\pi h_{em}}{Pc}, \tag{5}$$

where h_{em} is the emission height, P is the rotation period, and C is the speed of light (Blaskiewicz, Cordes, & Wasserman 1991; Dyks, Zhang, & Gil 2005). Nevertheless, the negative $\Delta\phi$ exhibited by PSR J1919+1745 leads to an unphysical negative emission height, which requires theoretical explanation by integrating two aspects: the positioning of the fiducial plane and the particularity of the emission region. Rookyard et al. (2015) indicated that the calculation of the emission height h_{em} depends on the reliability of $\Delta\phi$. The negative $\Delta\phi$ exhibited by J1919+1745 may result from the relatively dispersed pulse profile observed at the frequency of 1.25 GHz, which indirectly causes the mispositioning of $\phi_{\rm fid}$. For PSR J1730-3350 observed at a wavelength of 10 cm, the pulse profile becomes dispersed at longer wavelengths, which also leads to an unphysical negative emission height. A similar situation is observed for PSR J1648-4611 at the observation frequency of 1.4 GHz (Rookyard et al. 2015). If the negative $\Delta\phi$ of PSR J1919+1745 is not an observational bias, it may reflect a unique structure of its emission region. Different from the 'single open magnetic field line emission region' assumed in Rookyard et al. (2015), this pulsar might possess a localised emission region in the inner magnetosphere, which causes a reversal in the delay direction of the A/R effect.

Acknowledgement. This work made use of the data from Five-hundred-meter Aperture Spherical Radio Telescope (FAST). FAST is a Chinese national megascience facility, operated by National Astronomical Observatories, Chinese Academy of Sciences. This work is supported by National Natural Science Foundation of China (Nos. 12273008), the National SKA Program of China (Nos. 2022SKA0130100 and 2022SKA0130104), the Natural Science and Technology Foundation of Guizhou Province (No. [2023]024), the Foundation of Guizhou Provincial Education Department (No. KY (2020) 003).

Data Availability. The data underlying this article will be shared on reasonable request to the corresponding author.

References

Arons, J., & Barnard, J. J. 1986, 302, 120, doi: 10.1086/163978

Backer, D. C. 1970a, Natur, 228, 42, doi: 10.1038/228042a0

Backer, D. C. 1970b, Natur, 227, 692, doi: 10.1038/227692a0

Backer, D. C., Rankin, J. M., & Campbell, D. B. 1976, Natur, 263, 202, doi: 10.1038/263202a0

Basu, R., Mitra, D., & Melikidze, G. I. 2017, 846, 109, doi: 10.3847/1538-4357/aa862d

Basu, R., Mitra, D., & Melikidze, G. I. 2023, 947, 86, doi: 10.3847/1538-4357/acc6c6

Basu, R., et al. 2016, 833, 29, doi: 10.3847/1538-4357/833/1/29

Basu, R., Mitra, D., Melikidze, G. I., & Skrzypczak, A. 2019, 482, 3757, doi: 10.1093/mnras/sty2846

Bhattacharyya, B., Gupta, Y., & Gil, J. 2010, 408, 407, doi: 10.1111/j.1365-2966.2010.17116.x

Bhattacharyya, B., Gupta, Y., Gil, J., & Sendyk, M. 2007, 377, L10, doi: 10.1111/j.1745-3933.2007.00293.x

Biggs, J. D., McCulloch, P. M., Hamilton, P. A., Manchester, R. N., & Lyne, A. G. 1985, 215, 281, doi: 10.1093/mnras/215.2.281

Blaskiewicz, M., Cordes, J. M., & Wasserman, I. 1991, 370, 643, doi: 10.1086/169850

Cordes, J. M. 1975, 195, 193, doi: 10.1086/153318

Deneva, J. S., et al. 2009, 703, 2259, doi: 10.1088/0004-637X/703/2/2259

Deshpande, A. A., & Rankin, J. M. 2001, 322, 438, doi: 10.1046/j.1365-8711.2001.04079.x

Drake, F. D., & Craft, H. D. 1968, Natur, 220, 231, doi: 10.1038/220231a0

Dyks, J., Zhang, B., & Gil, J. 2005, 626, L45, doi: 10.1086/431651

Gil, J., Melikidze, G. I., & Geppert, U. 2003, 407, 315, doi: 10.1051/0004-6361:20030854

Gil, J. A., & Sendyk, M. 2000, 541, 351, doi: 10.1086/309394

Han, J. L., et al. 2025, RAA, 25, 014001, doi: 10.1088/1674-4527/ada3b7

Herfindal, J. L., & Rankin, J. M. 2007, 380, 430, doi: 10.1111/j.1365-2966.2007.12089.x

Herfindal, J. L., & Rankin, J. M. 2009, 393, 1391, doi: 10.1111/j.1365-2966.2008.14119.x

Hotan, A. W., van Straten, W., & Manchester, R. N. 2004, 21, 302, doi: 10.1071/AS04022

Janagal, P., Chakraborty, M., Bhat, N. D. R., Bhattacharyya, B., & McSweeney, S. J. 2022, 509, 4573, doi: 10.1093/mnras/stab3305

Jiang, P., et al. 2020, RAA, 20, 064, doi: 10.1088/1674-4527/20/5/64

Jones, P. B. 1981, 197, 1103, doi: 10.1093/mnras/197.4.1103

Maan, Y., & Deshpande, A. A. 2014, 792, 130, doi: 10.1088/0004-637X/792/2/130

Manchester, R. N., Hobbs, G. B., Teoh, A., & Hobbs, M. 2005, 129, 1993, doi: 10.1086/428488

Manchester, R. N., Taylor, J. H., & Huguenin, G. R. 1975, 196, 83, doi: 10.1086/153395

McSweeney, S. J., Bhat, N. D. R., Wright, G., Tremblay, S. E., & Kudale, S. 2019, 883, 28, doi: 10.3847/1538-4357/ab3a97

Qiao, G. J., & Lin, W. P. 1998, 333, 172, doi: 10.48550/arXiv.astro-ph/9708245

Radhakrishnan, V., & Cooke, D. J. 1969, ApL, 3, 225

Rahaman, S. k. M., Basu, R., Mitra, D., & Melikidze, G. I. 2021, 500, 4139, doi: 10.1093/mnras/staa3518

Rankin, J., & Rosen, R. 2014, 439, 3860, doi: 10.1093/mnras/stu237

Rankin, J. M. 1983, 274, 333, doi: 10.1086/161450

Rankin, J. M. 1993a, 85, 145, doi: 10.1086/191758

Rankin, J. M. 1993b, 405, 285, doi: 10.1086/172361

Rankin, J. M., & Wright, G. A. E. 2007, 379, 507, doi: 10.1111/j.1365-2966.2007.11980.x

Rejep, R., Wang, N., Yan, W. M., & Wen, Z. G. 2022, 509, 2507, doi: 10.1093/mnras/stab3063

Ren, X., et al. 2024, RAA, 24, 045010, doi: 10.1088/1674-4527/ad2dbe

Rookyard, S. C., Weltevrede, P., & Johnston, S. 2015, 446, 3367, doi: 10.1093/mnras/stu2236

Ruderman, M. A., & Sutherland, P. G. 1975, 196, 51, doi: 10.1086/153393

Smits, J. M., Mitra, D., & Kuijpers, J. 2005, 440, 683, doi: 10.1051/0004-6361:20041626

Szary, A., Melikidze, G. I., & Gil, J. 2015, 447, 2295, doi: 10.1093/mnras/stu2622

Szary, A., van Leeuwen, J., Weltevrede, P., & Maan, Y. 2020, 896, 168, doi: 10.3847/1538-4357/ab9226

Szary, A., et al. 2022, 934, 23, doi: 10.3847/1538-4357/ac75e2
Tedila, H. M., et al. 2022, 929, 171, doi: 10.3847/1538-4357/ac5f42
Tian, J., et al. 2024, 369, 21, doi: 10.1007/s10509-024-04284-9
Timokhin, A. N. 2010, 408, L41, doi: 10.1111/j.1745-3933.2010.00924.x
van Straten, W., & Bailes, M. 2011, 28, 1, doi: 10.1071/AS10021
van Straten, W., Demorest, P., & Oslowski, S. 2012, ART, 9, 237, doi: 10.48550/arXiv.1205.6276
Wang, N., Manchester, R. N., & Johnston, S. 2007, 377, 1383, doi: 10.1111/j.1365-2966.2007.11703.x
Wang, P. F., et al. 2020, 644, A73, doi: 10.1051/0004-6361/202038867
Weltevrede, P., Edwards, R. T., & Stappers, B. W. 2006, 445, 243, doi: 10.1051/0004-6361:20053088
Weltevrede, P., Stappers, B. W., & Edwards, R. T. 2007, 469, 607, doi: 10.1051/0004-6361:20066855
Wen, Z. G., et al. 2016, 592, A127, doi: 10.1051/0004-6361/201628214
Xu, X., et al. 2024a, 968, 119, doi: 10.3847/1538-4357/ad4889
Xu, X., et al. 2024b, 527, 3761, doi: 10.1093/mnras/stad3403
Xu, X., et al. 2025a, 989, 127, doi: 10.3847/1538-4357/adf1a1
Xu, X., et al. 2025b, 982, 117, doi: 10.3847/1538-4357/adbb65
Yuen, R. 2019, 486, 2011, doi: 10.1093/mnras/stz951
Zhang, B., Qiao, G. J., & Han, J. L. 1997, 491, 891, doi: 10.1086/304971
Zhi, Q., et al. 2023, 520, 1332, doi: 10.1093/mnras/stad235
Zhi, Q. J., et al. 2024, 960, 79, doi: 10.3847/1538-4357/ad0eca
Zhou, D. J., et al. 2023, RAA, 23, 104001, doi: 10.1088/1674-4527/accc76